Shaft Friction Characteristics of Two FRP Seawater Sea-sand Concrete Piles in a Rock-socket with or without Debris

Zejian Chen
Ph.D. Candidate, The Hong Kong Polytechnic University, Hong Kong SAR, China
Email: ze-jian.chen@connect.polyu.hk

Wen-Bo Chen (Corresponding Author)
Postdoctoral Fellow, The Hong Kong Polytechnic University, Hong Kong SAR, China
Email: geocwb@gmail.com

Jian-Hua Yin
Chair Professor, The Hong Kong Polytechnic University, Hong Kong SAR, China
Email: cejhyin@polyu.edu.hk

Numan Malik
Ph.D. Candidate, The Hong Kong Polytechnic University, Hong Kong SAR, China
Email: numan.malik@connect.polyu.hk

Manuscript submitted to *International Journal of Geomechanics*
as a Note

Abstract: The existence of debris at the bottom of a rock-socket significantly influences the mechanical behavior of a rock-socketed pile. To investigate the effects of debris on shaft friction and load transfer characteristics of a rock-socketed Fiber Reinforced Polymer (FRP) Seawater Sea-sand Concrete (SSC) pile, two physical model tests were conducted in this study. Cyclic and monotonic loadings were applied on the top of FRP-SSC model piles along axial direction. The vertical strains inside the model piles were monitored by embedded fiber Bragg grating sensors, which are used to calculate axial stress inside the pile and shaft friction at pile-rock interface. From the monitoring results, detailed distribution of load transfer and shaft friction in each model pile are obtained. Comparison of results from two model pile tests indicates that the shaft friction and the end-bearing stress were significantly influenced by the existence of debris at the bottom of the rock-socket. It is found that under cyclic loading and static loading, the mobilization of shaft friction is more dominant when debris existed than the case without debris. The end-bearing stress was reduced due to the existence of debris.

Keywords: rock-socketed piles, shaft friction, debris, fiber Bragg grating sensor, monotonic and cyclic loadings

1 Introduction

Rock-socketed bored piles are widely adopted to support high-rise buildings, due to large bearing capacity and small displacement under large external loading. The construction of rock socketed piles is time and labor consuming and therefore a suitable socket length should be determined. In many regional design codes (*e.g.* BS EN 1997; ACI 543R-2000; BD 2017), the pile capacity is estimated using empirical values and field test data. In Hong Kong's foundation code (BD 2017), the pile capacity is estimated using allowable side resistance and bearing stress of the rock socket, based on different rock grades. Since the interactions between rock socket and concrete pile remain unclear, conventional design of rock-socketed piles could be over-conservative and unreliable (Radhakrishnan and Leung 1989). Although reliable data were collected through field tests (*e.g.* Zhan and Yin 2000; Ng et al. 2001; Wang et al. 2019; Xu et al. 2019), ultimate pile capacity in a rock-socket was rarely reached due to the restrictions of loading conditions in the field tests with high cost in time and money. In laboratory-scale experiments, model piles are usually built with metal materials in cement mortar as replacement of rock sockets (Arshi and Stone 2011; Xing et al. 2014; Zhang et al. 2016; Wang and Chen 2019), instead of using actual materials in the fields. Shaft friction distribution along the socket length was less covered, which is especially complexed when debris exists at the pile bottom end. The existence of debris is usually inevitable after boring work and will significantly reduce the stiffness of the pile base and affect the mobilization of shaft and end resistance (Leong and Randolph 1994). To date, however, experimental study on the effect of debris on rock-socketed bored piles is rarely reported. Besides, structures especially in coastal areas are subjected to all kinds of cyclic loadings, generated by wind, sea wave, earthquakes, traffic, *etc*. The effect of lateral cyclic loadings on the piles had been extensively investigated in the earlier decades (Bea 1992). For axial cyclic effects, most of the studies were mainly focused on the cyclic behaviours of piles installed in sand or decomposed soils (Poulos 1989; Li et al. 2012). The effect of cyclic loading on the performance of rock-socketed bored piles is rarely discussed, especially the mobilization of shaft friction between the concrete pile and the rock socket.

To reveal the characteristics of shaft friction mobilization and the effect of debris of rock-socketed concrete piles under different axial loading conditions, physical model tests were conducted. Compared with in-situ tests, laboratory physical models have advantages in easy control of variables (such as forms of piles, stress conditions of soils and rock, installation method, *etc.*) and much lower cost (Sakr *et al*. 2004). Reduced scaled model piles were cast in a rock socket, with embedded fiber Bragg grating (FBG) sensors to measure strains inside the piles. Cyclic loadings were applied on the pile to simulate the dynamic loading conditions before the piles were monotonically loaded to failure. The shaft friction between the rock socket and the concrete and the load transfer modes of model piles with and without debris under increase of vertical loading and cycles numbers were presented and discussed.

2 Preparation of the physical model

2.1 Set-up of the physical model

The design of the physical model is shown in Fig.1. The model consists of a steel tank, an intact granite rock base, a model pile, and a hydraulic loading system. A socket with diameter of 100 mm and length of 160 mm was drilled at the center of the granite rock. The ratio of socket length to diameter 1.6 is within a common range in engineering practice (Ng *et al.* 2001; BD 2017). The rock base was fixed on the bottom of the steel tank by hardened gypsum plaster. The model was designed following geometry similarity. The similarity relations between the model and porotype is presented in Table 2, in which the value of n can be 6 to 25, as the diameter of full-scale piles can be 0.6 to 2.5m (Zhan and Yin 2001). The rock base was designed to be much larger than the piles to allow stresses spread in a similar way as in the field. The effects of gravity density and rate dependency were not considered in this study.

The pile was a novel composite structure using FRP reinforced seawater sea-sand concrete, which was proposed in recent years for marine constructions (Teng et al. 2011). Compared with conventional concrete piles reinforced by steel, the structure is expected to be more environmentally friendly with much higher resistance to seawater corrosion and comparable structural capacity (Mohamed et al. 2014; Ahmed et al. 2020). A Glass Fiber Reinforced Polymer (GFRP) rebar with diameter of 19mm was put at the center to simulate the reinforcement. GFRP is a corrosion-resistant material with high strength, which is getting popular in pile foundations especially in coastal areas (Guades et al. 2010). The concrete was cast inside the socket after installations of rebar and FBG arrays. Besides FBGs, an LVDT was installed on the cap of the pile to monitor the vertical pile head displacement under the axial loading. The external axial force was applied by a hydraulic actuator at the top of the frame and measured through the load cell fixed on the pile head, as shown in Fig.2.

2.2 Materials used for the physical model

The mix proportion of the SSC is shown in Table 1. The concrete is a novel type of seawater sea-sand concrete which is suitable for marine infrastructures with GFRP. Coarse aggregates were excluded from the mix to avoid scale effect in the small pile section. Fly ash and superplasticizer were added to increase the workability of the mixture. Uniaxial compression tests were conducted on three cylindrical specimens with diameter of 50mm and height of 100mm with strain gauges and the results are presented in Fig.3. The nonlinear ascending part of axial stress-strain curve was well fitted with the simplified formulation in CEB-FIP Model Code (CEB-FIP 1993), based on Sargin and Handa (1969)'s formulations, which is expressed in Eq. (1):

$$\frac{\sigma_{\mathrm{c}}}{f_{\mathrm{cm}}}=\frac{A\eta-\eta^{2}}{1+\left(A-2\right)\eta} \quad , \quad \text{with } \eta=\frac{\varepsilon_{\mathrm{c}}}{\varepsilon_{\mathrm{cm}}},\ A=\frac{E_{\mathrm{c}}}{f_{\mathrm{cm}}/\varepsilon_{\mathrm{cm}}} \tag{1}$$

where σ_c is the axial stress, ε_c is the axial strain, f_{cm} is the peak stress (f_{cm} = 31 MPa), ε_{cm} is the strain at f_{cm} (ε_{cm} = 0.00344) and E_c is the initial elastic modulus (E_c = 22.9 GPa). It is clear that the tangent modulus $E_{\mathrm{t}}=\frac{\mathrm{d}\sigma_{\mathrm{c}}}{\mathrm{d}\varepsilon_{\mathrm{c}}}$ was non-constant according to Eq. (1). Combined with axial strain measured by FBG sensors, Eq. (1) was used to calculate the axial stress of the concrete inside the rock socket in this study.

The GFRP rebars are assumed linear elastic materials with a Young's modulus of 50 GPa according to the manufacturer's report. Six core samples made from the granite rock were prepared for uniaxial compressive tests. The average uniaxial compressive strength (UCS) was found to be around 177 MPa and the Young's modulus (E) was around 42 GPa. Uniaxial compression tests were also conducted on hardened gypsum plaster in which UCS = 60 MPa and E = 22 GPa.

2.3 Instrumentation by multiplexed FBGs

FBG has the advantages of light weight, high frequency, good resistance to electromagnetic interference and high resolution, which has been growingly popular in recent years in geotechnical engineering (Hong et al. 2016; Kister et al. 2007; Pei et al. 2014; Chen et al. 2020). In this study, application of FBGs allows less occupation of space inside the pile, high resolution of strain measurement and high frequency of data acquisition under cyclic loadings, which is difficult to achieve with conventional strain gauges.

Arrays of multiplexed FBG sensors were put inside the pile, including one attached on the rebar surface and the rest on two special aluminum channels, as shown in Fig. 1. The aluminum channel has a U-shape section and was embedded in the concrete. The aluminum channels aimed to protect the vulnerable optical fiber and to form a quasi-distributed sensing strip with finite numbers of FBGs on it. With input of a broad band incident light into the optical fiber, the central light wavelength reflected by the grating region will shift with changes of local strain and temperature. The correlation between wavelength, strain and temperature follows Eq. (2):

$$\frac{\Delta\lambda_{\mathrm{i}}}{\lambda_{\mathrm{i}}} = c_1\Delta\varepsilon_{\mathrm{i}} + c_2\Delta T_{\mathrm{i}} \tag{2}$$

where λ_{i} is the initial reflected wavelength of the FBG, $\Delta\lambda_{\mathrm{i}}$ is the increment of λ_{i}, c_1 and c_2 are constants, $\Delta\varepsilon_{\mathrm{i}}$ is the incremental longitudinal strain, and ΔT_{i} is the change of local temperature. In this study, c_1 was taken as 0.78 (Pei et al. 2014) and the term with c_2 in is omitted since temperature variation could be neglected during the laboratory tests.

FBG sensors were placed at five different positions inside the pile, as shown in Fig.1. The distance between adjacent FBGs was 35mm. The shaft resistance provided by the rock socket was calculated by Eq. (3):

$$f = \frac{\Delta F}{\Delta h \cdot \pi \cdot D} = \frac{\Delta\sigma_{\mathrm{c}} A_{\mathrm{c}} + \Delta\sigma_{\mathrm{f}} A_{\mathrm{f}}}{\Delta h \cdot \pi \cdot D} \tag{3}$$

where f is the average shaft friction between two measuring points, $\Delta\sigma_{\mathrm{c}}$ is difference of stress, A is the section area of the material, subscripts c and f represent the concrete and the FRP respectively, Δh is the distance between the two sensors and D is the pile diameter. To calculate the incremental axial stress with incremental strains, the FRP was treated as an elastic material while the concrete was regarded as a nonlinear elastic-plastic material, using the tangent modulus E_{t} by the stress-strain curve in 2.2.

2.4 Test program of the model piles

In this study, two model piles as shown in Fig.1 (a) and (b) were prepared and tested. The first model pile (Pile 1) was directly cast inside the rock socket after clearing the drilled hole. For the second model pile (Pile 2), a 10mm-thick layer of loose debris (consisting completely decomposed soils and fine aggregates with diameter < 10 mm) was placed at the bottom of the socket before casting of concrete. Its composition and state are similar to the in-situ debris, which is usually formed by drilling work in the soil layers and bedrock and deposition under gravity. Other conditions were kept unchanged for the two piles.

The piles were kept wet with seawater for curing for the same period as in the uniaxial compression tests. Cyclic loadings were then applied following a sine function started at 60kN with amplitudes of 60 kN for 1000 cycles before the monotonic loading. The frequency of cyclic loading was 0.2 Hz, which is commonly met with in marine infrastructures. After completion of cyclic loading, the piles were unloaded to the origin and then compressed monotonically until failure under load control, at a speed of +0.3 kN/s.

3 Test results

3.1 Load transfer between the pile and rock socket

The peak load $Q_{\max}$ of Pile 1 and Pile 2 were 239kN and 208kN respectively, and the failure happened at the pile body outside the rock socket, indicating the high capacity provided by the rock socket. For engineering application, if the rock socket capacity is higher than the structural capacity, the socket length might be overconservative and could be reduced. Fig.4 shows the load percentage undertaken by the shaft and base respectively with the increase of static loading Q. It is demonstrated that the shaft resistance accounted for more than 85% to 90% of the total resistance for Pile 1. However, the contribution of shaft resistance of Pile 2 was more significant and tended to increase with rising of Q, ranging from around 90% to 95%. According to the elastic solutions by Pells and Turner (1979), the shaft resistance of the rock-socketed piles in this study ($E_{\mathrm{pile}}/E_{\mathrm{rock}} = 0.55$ and $L / D=1.6$) contributed around 89% of the total axial force. In Fig.4, the shaft resistance of Pile 1 was highly close to Pells and Turner's solution, while shaft resistance of Pile 2 was slightly higher, probably due to the lower stiffness under the pile base caused by the debris. The fluctuations of curves were much more obvious for Pile 2 as well.

Fig.5 presents the axial forces at different depths along rock socket under Q=200kN. It is clearly shown that the percentage of axial load transferred to the lower part of rock socket is smaller in Pile 2 compared with Pile 1. The axial force at the bottom end of Pile 2 is only 10 kN under external loading of 200 kN. At the upper part however, the axial force of Pile 1 was slightly lower compared with Pile 2. It should be noted that the axial forces at depth of 0mm indirectly measured by FBGs were much smaller than 200 kN for both piles. The main reason is that the FBG has a length of 10mm and its strain value was probably influenced by a small section inside the rock socket, which is significantly reduced by the local shaft friction. This can also be possibly explained by a stuck effect from rock surface on the pile, since the pile diameter might not be perfectly identical with the bored hole due to complexity of manufacturing.

3.2 Shaft friction mobilization in the rock socket

Fig.6 shows the mobilized shaft friction f between the rock socket and the pile at different sections under monotonic loading, which is calculated according to the axial force differences. The curves in Fig.6 for Pile 1 are highly linear, while the nonlinearity and fluctuations are obvious for Pile 2. Shaft friction generally increases with applied force Q, the maximum values of which reached up to 7-8 MPa near the rock surface, which was probably due to stuck effect by the drill hole. The maximum friction at the lower parts was also high, mostly ranging from 3 to 6 times of the allowable maximum frictional resistance (0.7 MPa) in Hong Kong's design code (BD 2017). According to the formula summarized by Kulkarni and Dewaikar (2017, 2019), the limit skin friction of the model piles could be estimated as $f_{\max} = 0.2\sigma_{\mathrm{cm}}^{0.5} = 2.67\mathrm{MPa}$, which is lower than the maximum measured ones in this study, indicating that conventional design could be over-conservative for concrete piles in intact granite rock socket.

Besides, the mobilized shaft frictions of Pile 2 were generally higher than the friction of Pile 1 by around 10% to 100% at the three upper sections from 0 to 105mm in depth, except for the lowest section, where the shaft friction was kept low. Therefore, the existence of debris did intensify the mobilization of shaft resistance especially at the shallower parts.

Fig.7 shows the distribution of shaft friction along the socket depth under Q=200kN. On general, the friction gradually decreased with depth for both piles, which was more significant for Pile 2. The ratio of shaft friction of Pile 2 to Pile 1 were around 1.1 at 22.5 mm, 1.75 at 62.5 mm, 1.48 at 87.5 mm and 0.32 at 122.5 mm in depth. In another word, the debris under Pile 2 increased the concentration of shaft friction at the shallower parts of rock socket.

3.3 Shaft friction mobilization under cyclic loadings

Cyclic loading was applied axially on the pile head before the final monotonic loading to failure. The cyclic loading followed a sine function with initial load of 60 kN, amplitude of 60 kN and frequency of 0.2 Hz. In Fig.8, the curves represent the mean values of average shaft resistance f_{m} along the whole socket length under 60kN, with increase of the cycle number. The mean friction gradually increases by around 16% for Pile 1 and 34% for Pile 2 respectively after 1000 cycles. However, since the ultimate friction provided by the rock socket is unlikely to increase, the growth of friction implied reduction of the actual safety factor of the rock socket under cyclic loading.

Growth of mobilized shaft friction is closely related to the increase of relative displacement between pile and rock and the reduction of pile base resistance, due to the deterioration of concrete under cyclic loading. It is also clearly shown that the increase of mean shaft friction of Pile 2 is faster compared with Pile 1, indicating that the existence of drill hole debris will intensify the cyclic effect on shaft resistance mobilization. This effect is probably due to the deterioration of debris, such as crushing and collapse of particles at the base of the pile under loading cycles. Compaction effect seemed insignificant in either the debris or rock as well, as the displacements were small. However, there was no significant difference between the friction amplitudes of the two piles, which indicated that debris has little effect on the cyclic friction amplitude.

4 Conclusions

This note provides a physical model investigation on the load transfer and shaft friction between FRP reinforced concrete piles and rock socket. Multiplexed FBG sensors were embedded inside the pile to measure the distribution of axial strains and a nonlinear concrete model was adopted to calculate the corresponding axial stress and shaft friction. The effect of debris and cyclic loading were also involved and discussed. Several conclusions can be drawn from the test results.

(1) Although the failure did not occur at the rock-pile interface, the mobilization of shaft friction between the model pile and the intact granite rock socket is found significant under axial loading, which could be underestimated in conventional design.

(2) The existence of debris inside the rock socket results in smaller stiffness of pile base and larger relative displacement, which increases shaft friction mobilization by 10% to 100% at the shallower parts. The contribution percentage of base resistance to the total capacity is decreased from 10-15% to 5-10% by the debris. It is inferred that such rock

socketed piles rely severely on the shaft friction especially with debris in the field condition. In engineering design, the shaft resistance may be considered as a dominant contributor, however, with suitable reduction of safety factor for existence of debris.

(3) The mobilized shaft friction gradually increases with loading cycles under cyclic loading, while the amplitude of friction is almost unchanged, for both two piles. Under 1000 loading cycles, the pile with debris (friction increased by 34%) was more sensitive to cyclic loading effect in friction mobilization compared with the other one (friction increased by 16%). It is recommended to adopt a higher margin of shaft friction for considerations of cyclic loading and debris effect in rock socketed pile design.

(4) The physical model tests provide valuable data on capturing the behaviours of FRP reinforced concrete piles in granite rock socket. Although it is a reduced-scale model tests, the results can be used to verify numerical methods, which can be extended to predictions of full-scale piles in the fields. There are also rooms for further experimental or numerical studies on investigating different impact factors on the shaft friction, such as rock strength, scale effect, thickness of debris, etc.

Data Availability Statement

All data, models, and code generated or used during the study appear in the submitted article.

Acknowledgement

The work in this paper is supported by a Theme-based Research Scheme project (T22-502/18-R), a Research Impact Fund (RIF) project (R5037-18) and two GRF projects (PolyU 152796/16E, PolyU 152209/17E) from Research Grants Council (RGC) of Hong Kong Special Administrative Region Government of China. The authors also acknowledge the financial supports from Research Institute for Sustainable Urban Development of The Hong Kong Polytechnic University and a grant (ZDBS) from The Hong Kong Polytechnic University.

References

ACI 543R-2000. (2000). “Design , Manufacture , and Installation of Concrete Piles.” *Reported by American Concrete Institute Committee*.

Ahmed, A., Guo, S., Zhang, Z., Shi, C., & Zhu, D. (2020). A review on durability of fiber reinforced polymer (FRP) bars reinforced seawater sea sand concrete. *Construction and Building Materials*, *256,* 119484.

Arshi, H., and Stone, K. J. (2011). “An investigation of a rock socketed pile with an integral bearing plate founded over weak rock.” *15th European Conference on Soil Mechanics and Geotechnical Engineering: Geotechnics of Hard Soils - Weak Rocks: 2011*.

Bea, B. R. G. (1992). “PILE CAPACITY FOR AXIAL CYCLIC LOADING.” *J. Geotech. Engrg.*, 118(1), 34–50.

BSI. (2004). “BS EN 1997-1: Eurocode 7: Geotechnical design - Part 1: General rules.”

Buildings Department Technical Committee of Hong Kong (BD). (2017). *Code of Practice for Foundations 2017*. of Hong Kong.

CEB-FIP. (1993). *CEB-FIP model code 1990 - Design Code*. *Bulletin d’Information 213/214*.

Chen, W. B., Feng, W. Q., Yin, J. H., and Qin, J. Q. (2020). “New FBG-based device for measuring small and large radial strains in triaxial apparatus.” *Canadian Geotechnical Journal,* https://doi.org/10.1139/cgj-2020-0145

Guades, E., Aravinthan, T., and Islam, M. M. (2010). “An overview on the application of FRP composites in piling system.” *Proceedings of the Southern Region Engineering Conference (SREC 2010),* Engineers Australia, 65–70.

Hong, C. Y., Zhang, Y. F., Zhang, M. X., Leung, L. M. G., and Liu, L. Q. (2016). “Application of FBG sensors for geotechnical health monitoring, a review of sensor design, implementation methods and packaging techniques.” *Sensors and Actuators, A: Physical*, Elsevier B.V., 244, 184–197.

Kister, G., Winter, D., Gebremichael, Y. M., Leighton, J., Badcock, R. A., Tester, P. D., Krishnamurthy, S., Boyle, W. J. O., Grattan, K. T. V., and Fernando, G. F. (2007). “Methodology and integrity monitoring of foundation concrete piles using Bragg grating optical fibre sensors.” *Engineering Structures*, 29(9), 2048–2055.

Kulkarni, R. U., and Dewaikar, D. M. (2017). “An empirical approach to assess socket friction and point resistance of axially loaded rock-socketed piles of Mumbai region.” *International Journal of Geotechnical Engineering*.

Kulkarni, R. U., and Dewaikar, D. M. (2019). “Analysis of rock-socketed piles loaded in axial compression in Mumbai region based on load transfer characteristics.” *International Journal of Geotechnical Engineering*, Taylor & Francis, 13(3), 261–269.

Leong, E. C., and Randolph, M. F. (1994). “Finite element modelling of rock-socketed piles.” *International Journal for Numerical and Analytical Methods in Geomechanics*, 18, 25–47.

Li, Z., Bolton, M. D., and Haigh, S. K. (2012). “Cyclic axial behaviour of piles and pile groups in sand.” *Canadian Geotechnical Journal*, 49(9), 1074–1087.

Mohamed, H. M., Afifi, M. Z., and Benmokrane, B. (2014). Performance evaluation of concrete columns reinforced longitudinally with FRP bars and confined with FRP hoops and spirals under axial load. *Journal of Bridge Engineering*, *19*(7), 04014020.

Ng, C. W. W., Yau, T. L. Y., Li, J. H. M., and Tang, W. H. (2001). “SIDE RESISTANCE OF LARGE DIAMETER BORED PILES SOCKETED INTO DECOMPOSED ROCKS.” *J. Geotech. Geoenviron. Eng.*, 127(8), 642–657.

Pei, H. F., Teng, J., Yin, J. H., and Chen, R. (2014). “A review of previous studies on the applications of optical fiber sensors in geotechnical health monitoring." *Measurement: Journal of the International Measurement Confederation*, Elsevier Ltd, 58, 207–214.

Pells, P. J., and Turner, R. M. (1979). "Elastic Solutions for the Design and Analysis of Rock-Socketed Piles." *Canadian geotechnical journal*, 16(3), 481–487.

Poulos, H. G. (1989). "CYCLIC AXIAL LOADING ANALYSIS OF PILES IN SAND." *J. Geotech. Engrg.*, 115(6), 836–852.

Radhakrishnan, R., and Leung, C. F. (1989). "Load transfer behavior of rock-socketed piles." *J.Geotech.Engrg.*, 115(6), 755–768.

Sakr, M., Naggar, M. H. E., & Nehdi, M. (2004). Novel toe driving for thin-walled piles and performance of fiberglass-reinforced polymer (FRP) pile segments. *Canadian geotechnical journal*, *41*(2), 313-325.

Sargin, M., and Handa, V. K. (1969). *A General Formulation for the Stress-Strain Properties of Concrete. Solid Mechanics Division, University of Waterloo*.

Xing, H., Zhang, Z., Meng, M., Luo, Y., and Ye, G. (2014). "Centrifuge tests of superlarge-diameter rock-socketed piles and their bearing characteristics." *Journal of Bridge Engineering*, 19(6), 1–10.

Wang, H. L., and Chen, R. P. (2019). "Estimating static and dynamic stresses in geosynthetic-reinforced pile-supported track-bed under train moving loads." *J. Geotech. Geoenviron. Eng.*, 145 (7): 04019029.

Wang, H. L., Chen, R. P., Cheng, W., Qi, S., and Cui, Y. J. (2019). "Full-scale model study on variations of soil stress in the geosynthetic-reinforced pile-supported track-bed with water level change and cyclic loading." *Can. Geotech. J.*, 56 (1): 60–68.

Xu, D. S., Xu, X. Y., Li, W., Fatahi B. (2019). "Field experiments on laterally loaded piles for an offshore wind farm" *Marine Structures*, 69: 102684.

Zhan, C., and Yin, J.-H. (2000). “Field static load tests on drilled shaft founded on or socketed into rock.” *Canadian Geotechnical Journal*, 37(6), 1283–1294.

Zhang, B. J., Huang, B., Mei, C., Fu, X. D., Luo, G., and Yang, Z. J. (2016). “Dynamic Behaviours of a Single Soft Rock-Socketed Shaft Subjected to Axial Cyclic Loading.” *Advances in Materials Science and Engineering*, 2016.

Figure caption list

Fig.1 The set-up and dimensions of the physical model (S0 to S5 are the FBG sensors and inside the blanket is the initial wavelength): (a) Pile 1; (b) Pile 2; (c) cross-section of the model pile

Fig.2 Photos of the physical model: (a) the loading system and steel tank; (b) the model pile inside the tank

Fig.3 The measured and fitted compressive stress-strain curves and tangent modulus E_t of the concrete

Fig.4 The bearing percentage by shaft and base resistance of two FRP-SSC model piles under increasing axial load

Fig.5 The load transfer in the rock socket of two FRP-SSC model piles under axial load of 200kN

Fig.6 Development of shaft friction at different positions under increasing axial loading (the numbers in the legend represent the two edge points of the section. *e.g*. "0-45" means the section between 0mm and 45 mm in depth below the rock surface)

Fig.7 Shaft friction distribution of two FRP-SSC model piles under axial load of 200kN

Fig.8 The mean values of shaft friction of two FRP-SSC model piles under cyclic loading

Tables

Table 1 Mix ratios of SSC

Cement	Fly ash	Seawater	Sea-sand	Superplasticizer
1	0.33	0.8	4.33	0.013

(Example: mix ratio of fly ash is mass of fly ash/mass of cement=0.33)

Table 2 Similarity rate of the physical model

Physical quantity	Dimension	Model / Porotype	Physical quantity	Dimension	Model / Porotype
Length of pile	L	$1 / n$	Strength	$ML^{-1}T^{-2}$	1
Diameter of pile	L	$1 / n$	Young's modulus	$ML^{-1}T^{-2}$	1
Area	L^2	$1/ n^2$	Shear modulus	$ML^{-1}T^{-2}$	1
Axial force	MLT^{-2}	$1/ n^2$	Stress	$ML^{-1}T^{-2}$	1
Displacement	L	$1/ n$	Strain	-	1

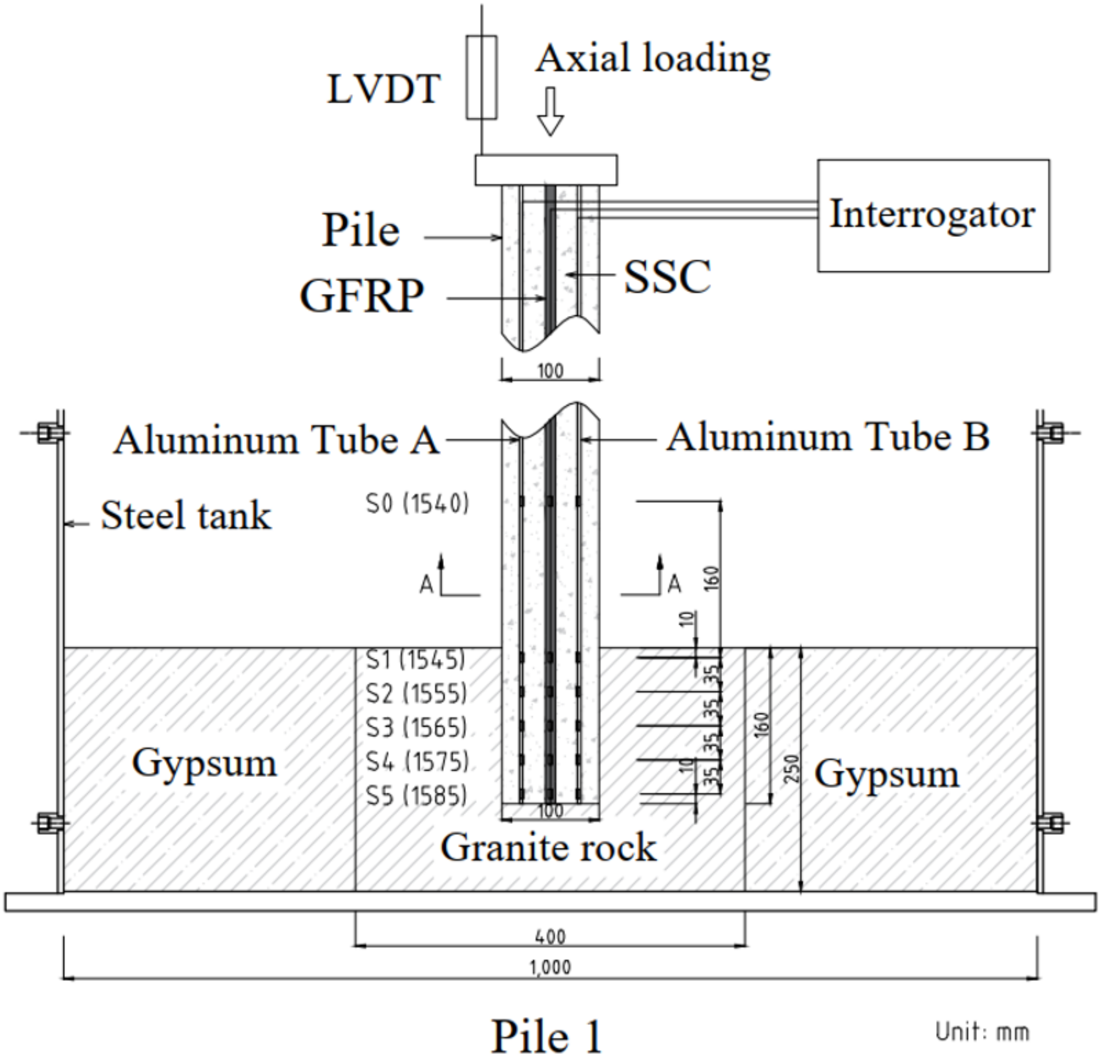
LVDT
Axial loading
Interrogator
Pile
GFRP
SSC
100
Aluminum Tube A
Aluminum Tube B
Steel tank
S0 (1540)
A
A
160
10
S1 (1545)
S2 (1555)
S3 (1565)
S4 (1575)
S5 (1585)
35
35
35
35
10
160
250
Gypsum
Gypsum
100
Granite rock
400
1,000
Pile 1
Unit: mm

(a)

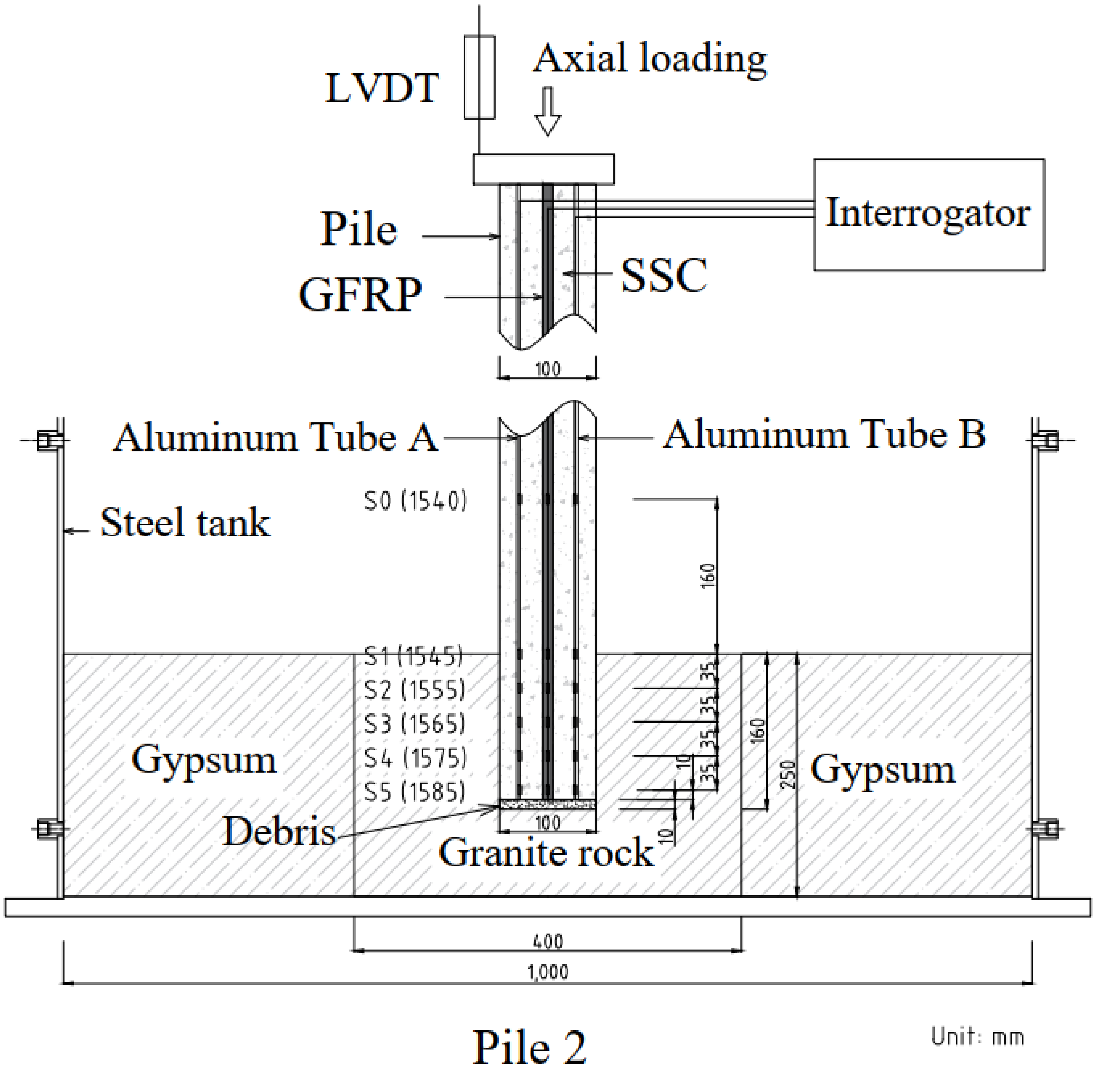
LVDT
Axial loading
Interrogator
Pile
GFRP
SSC
100
Aluminum Tube A
Aluminum Tube B
Steel tank
S0 (1540)
160
S1 (1545)
S2 (1555)
S3 (1565)
S4 (1575)
S5 (1585)
35
35
35
35
10
10
160
250
Gypsum
Gypsum
Debris
100
Granite rock
400
1,000
Pile 2
Unit: mm

(b)

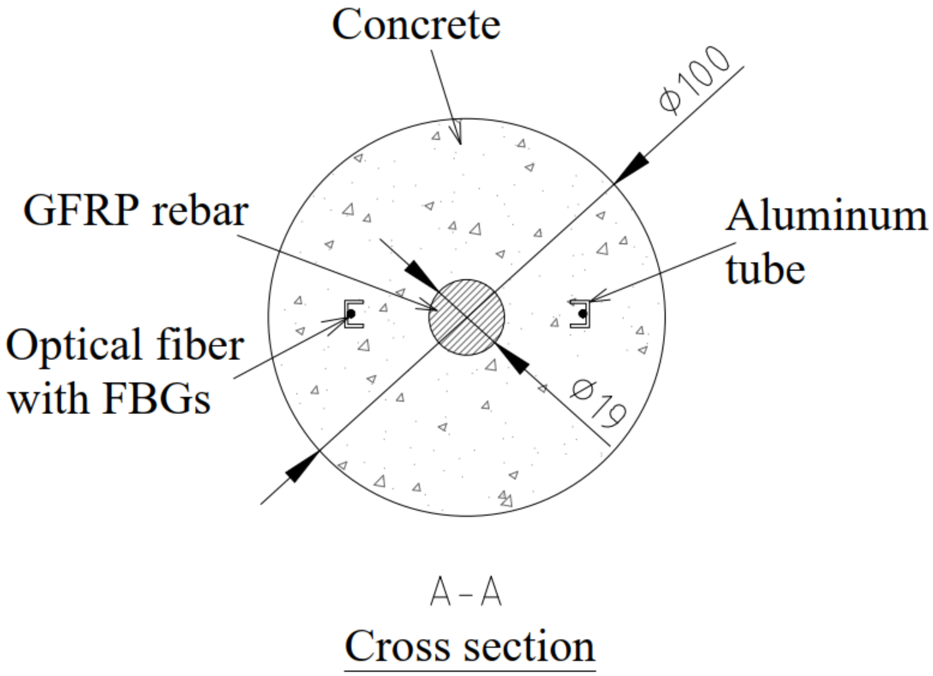
Concrete
ϕ100
GFRP rebar
Aluminum
tube
Optical fiber
with FBGs
ϕ19
A-A
Cross section

(c)

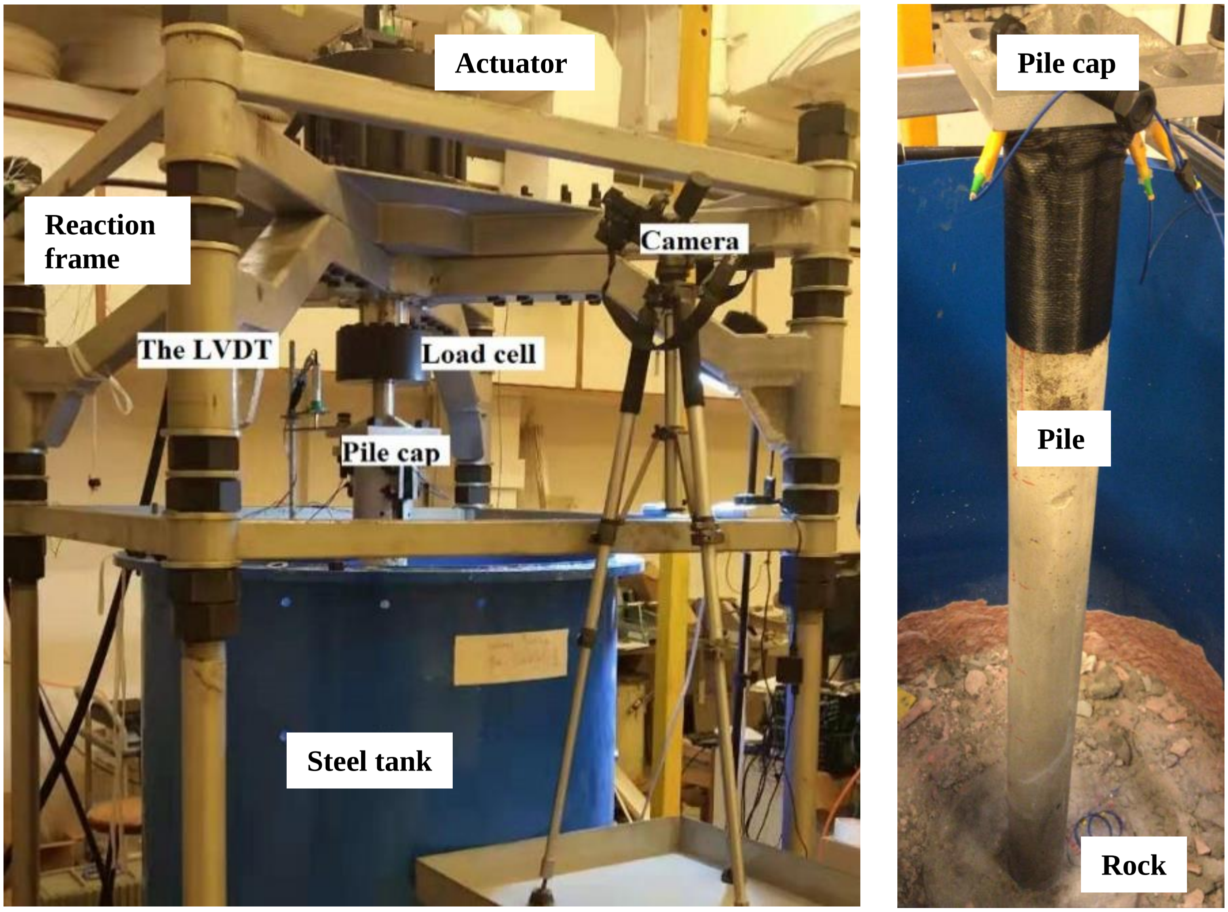
Actuator
Reaction frame
Camera
The LVDT
Load cell
Pile cap
Steel tank
Pile cap
Pile
Rock

(a) (b)

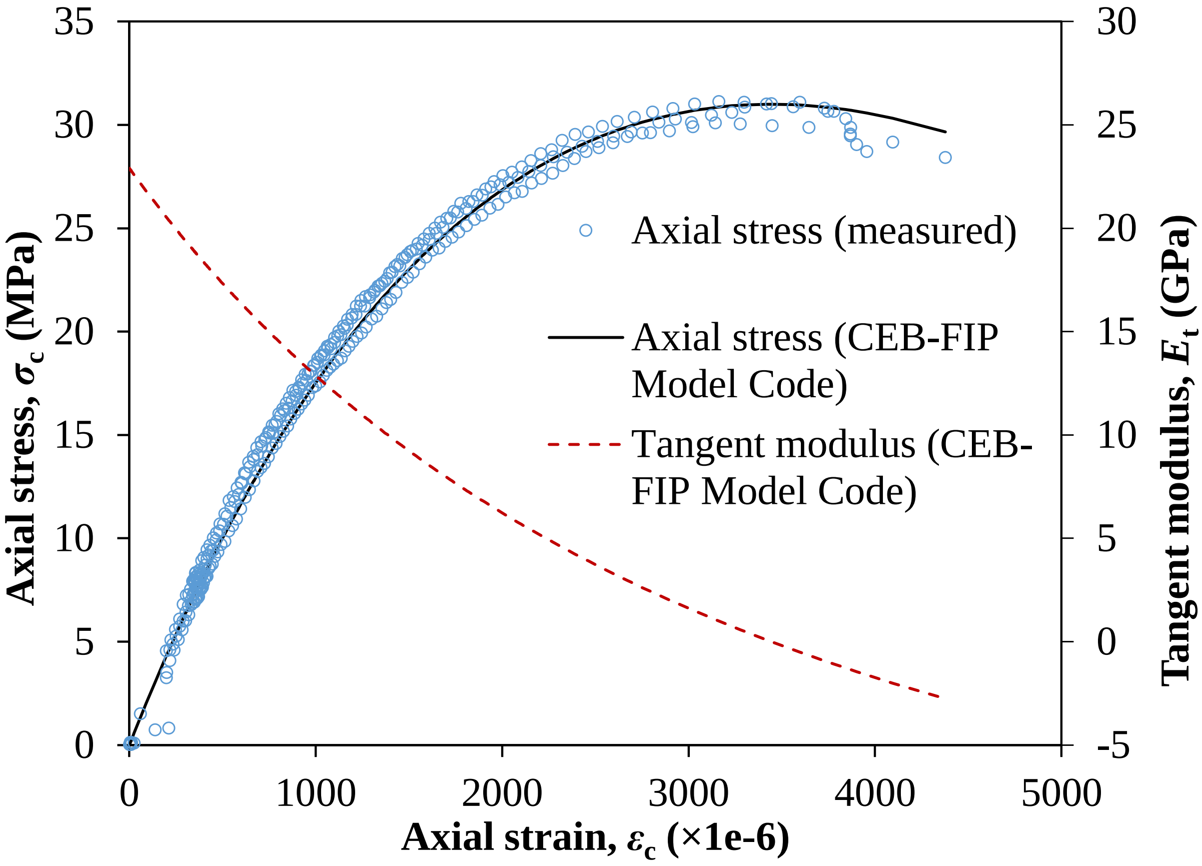
Axial stress (measured)
Axial stress (CEB-FIP Model Code)
Tangent modulus (CEB-FIP Model Code)
Axial stress, σ_c (MPa)
Tangent modulus, E_t (GPa)
Axial strain, ε_c (×1e-6)
0
5
10
15
20
25
30
35
-5
0
5
10
15
20
25
30
0
1000
2000
3000
4000
5000

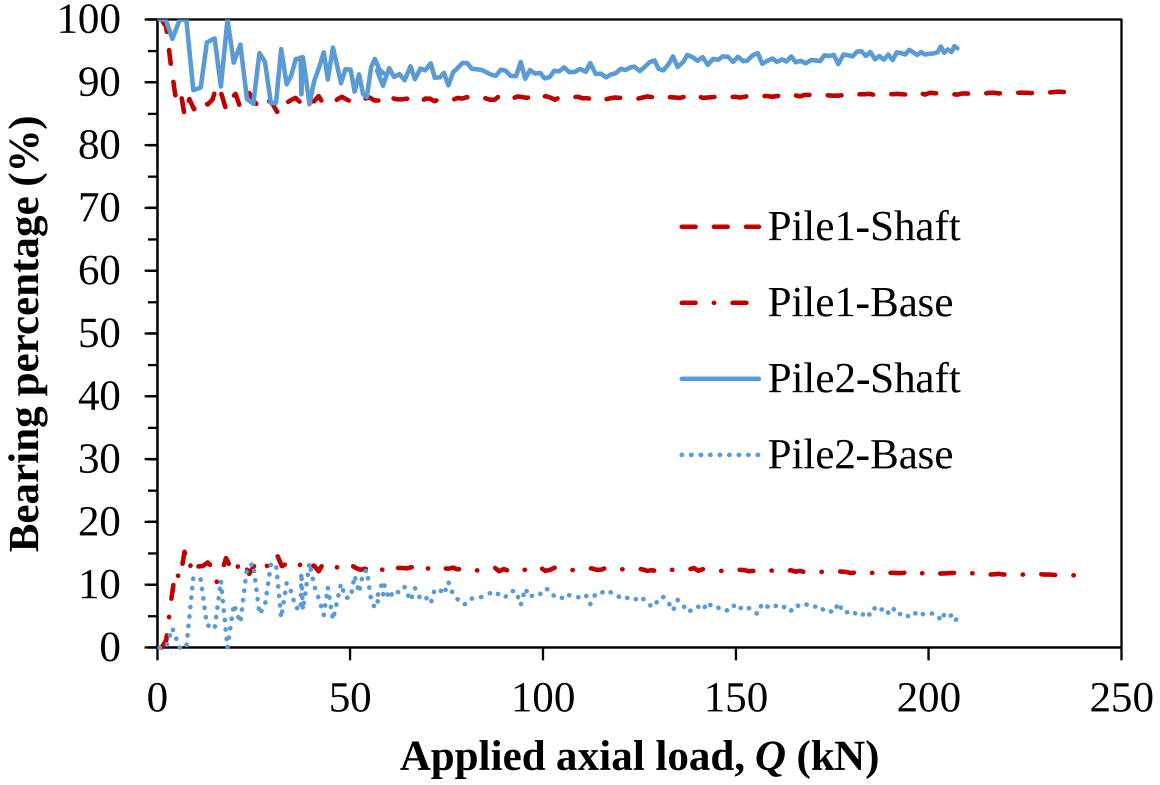
100
90
80
70
60
50
40
30
20
10
0
Bearing percentage (%)
0
50
100
150
200
250
Applied axial load, *Q* (kN)
Pile1-Shaft
Pile1-Base
Pile2-Shaft
Pile2-Base

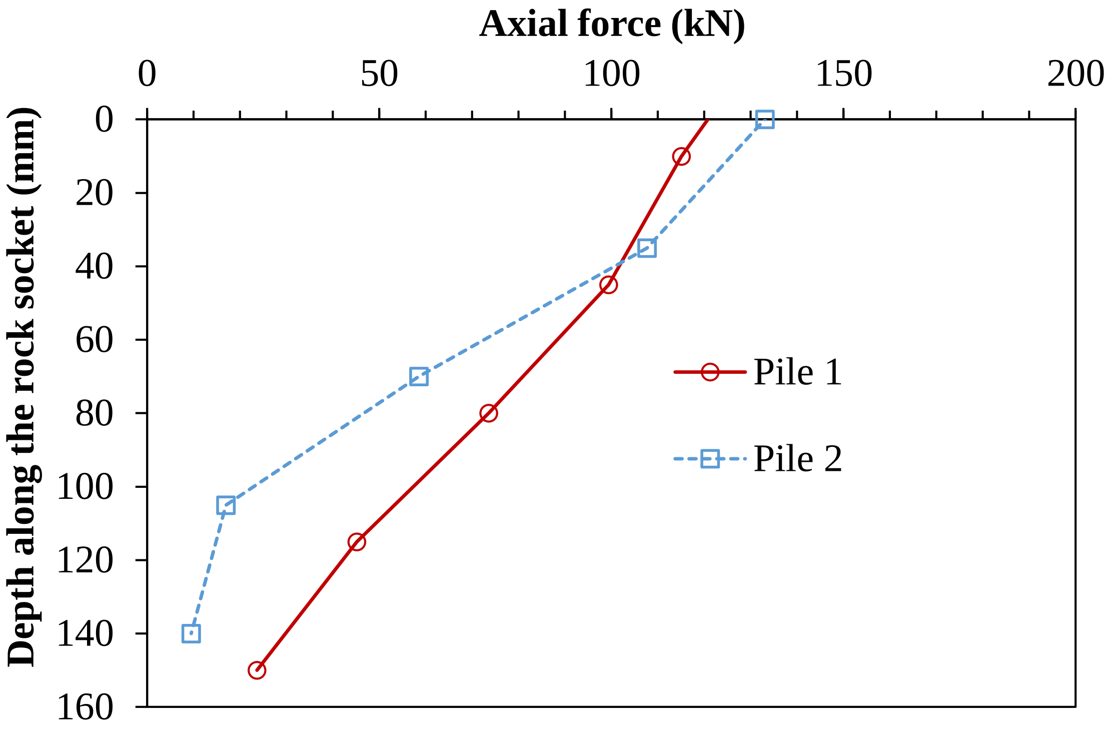
Axial force (kN)
0
50
100
150
200
Depth along the rock socket (mm)
0
20
40
60
80
100
120
140
160
Pile 1
Pile 2

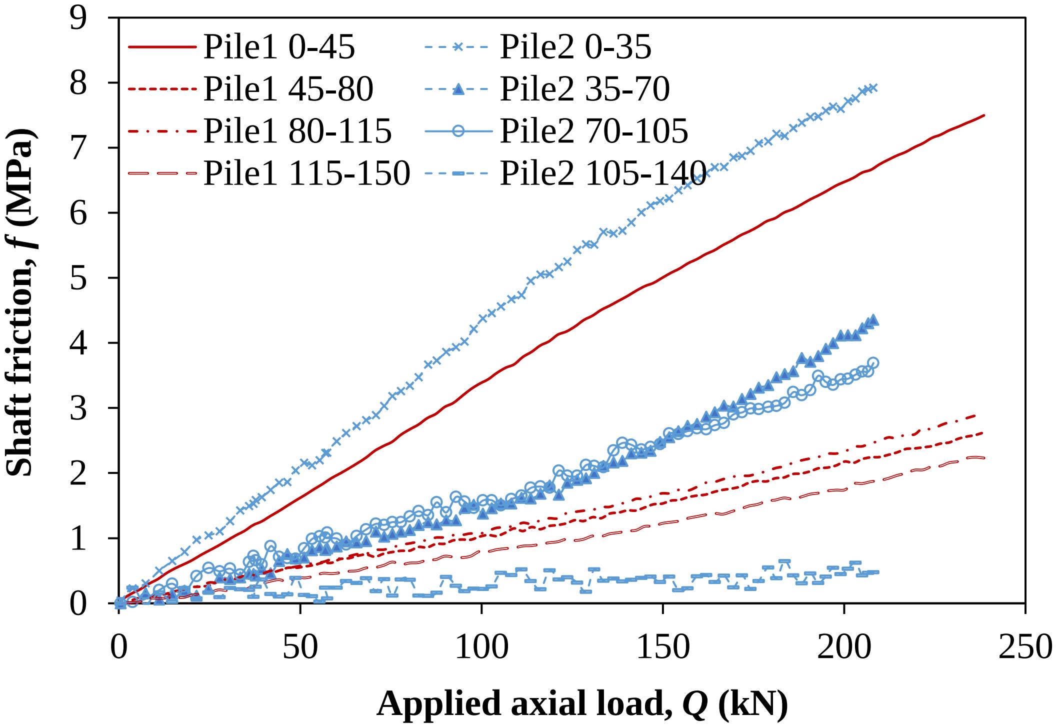

Shaft friction, f (MPa)
0
1
2
3
4
5
6
7
8
9
Applied axial load, Q (kN)
0
50
100
150
200
250
Pile1 0-45
Pile1 45-80
Pile1 80-115
Pile1 115-150
Pile2 0-35
Pile2 35-70
Pile2 70-105
Pile2 105-140

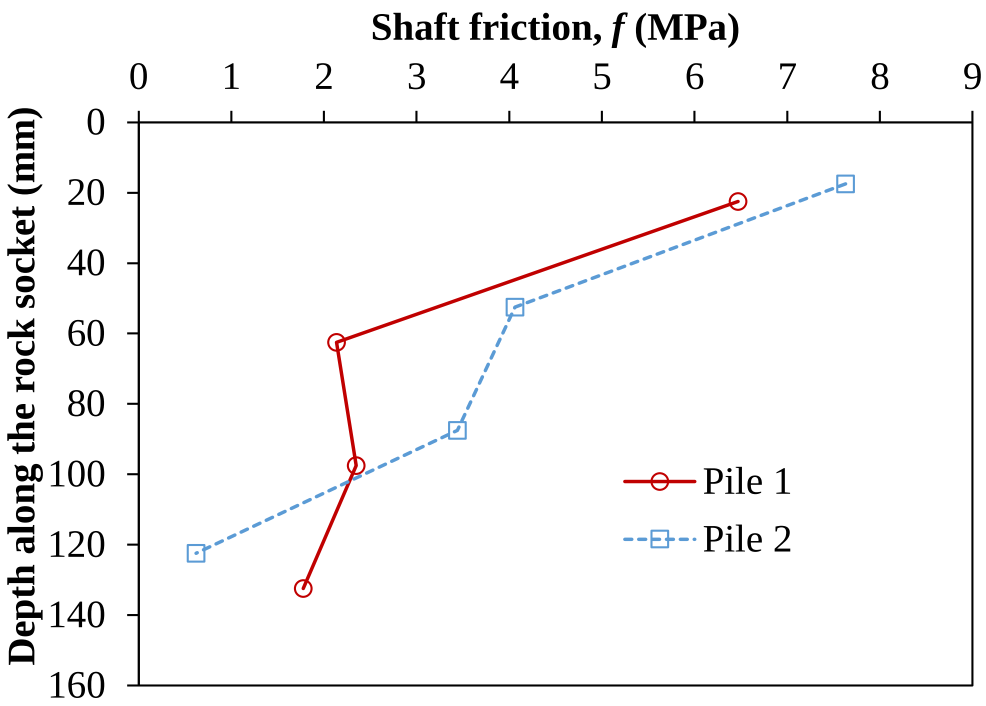
Shaft friction, f (MPa)
0
1
2
3
4
5
6
7
8
9
Depth along the rock socket (mm)
0
20
40
60
80
100
120
140
160
Pile 1
Pile 2

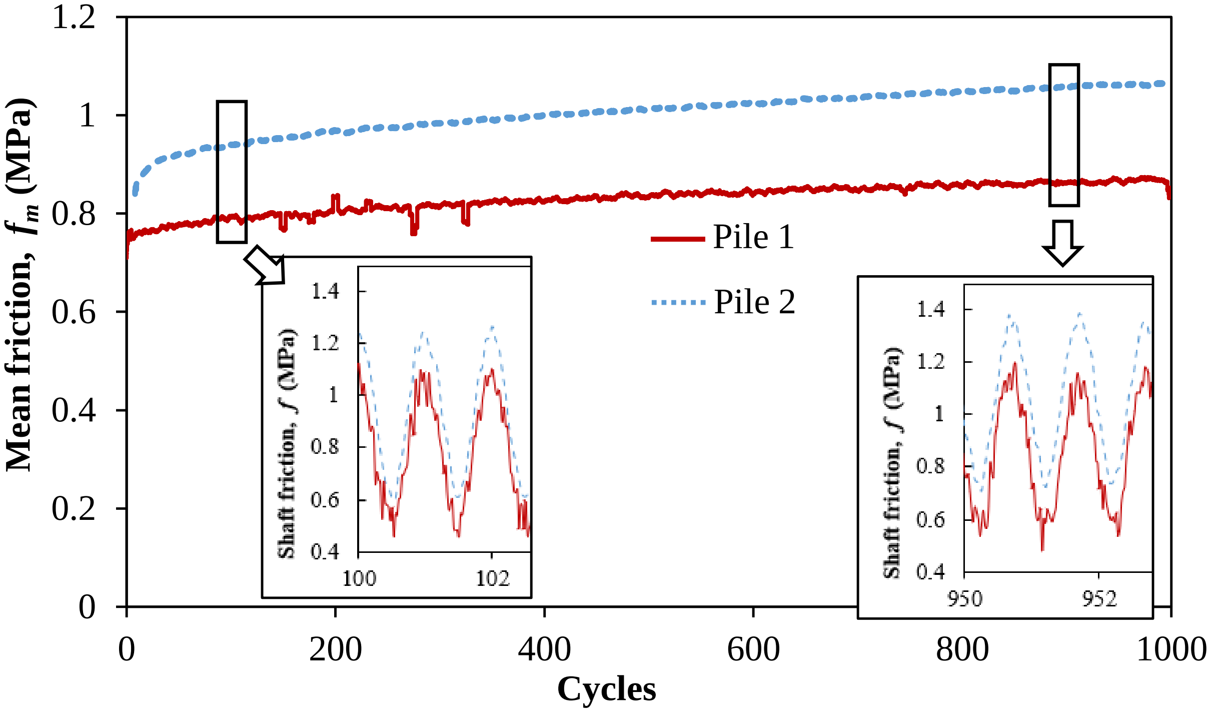

Mean friction, f_m (MPa)
1.2
1
0.8
0.6
0.4
0.2
0
0
200
400
600
800
1000
Cycles
Pile 1
Pile 2
Shaft friction, f (MPa)
1.4
1.2
1
0.8
0.6
0.4
100
102
950
952